## Title
On the exceptional damage-tolerance of gradient metallic materials



## Authors
Cao, R
Yu, Q
Pan, J
et al.

## Publication Date
2020

## DOI
10.1016/j.mattod.2019.09.023

Peer reviewed

# On the Exceptional Damage-Tolerance of Gradient Metallic Materials

**Ruqing Cao[1,2+], Qin Yu[3+], Jie Pan[1], Yan Lin[1], Andrew Sweet[3,4], Yi Li[1*] and Robert O. Ritchie[3,4*]**

[1]Shenyang National Laboratory for Materials Science, Institute of Metal Research, Chinese Academy of Sciences, Shenyang 110016, China

[2]School of Materials Science and Engineering, University of Science and Technology of China, Hefei 230026, China

[3]Materials Sciences Division, Lawrence Berkeley National Laboratory, Berkeley, CA 94720, USA

[4]Department of Materials Science & Engineering, University of California, Berkeley, CA 94720, USA

*Corresponding authors: Y. Li (liyi@imr.ac.cn) and R. O. Ritchie (roritchie@lbl.gov)

+These authors contributed equally to this work.

## Abstract

An experimental study is described on the fracture toughness and micro-mechanisms associated with the initiation and propagation of cracks in metallic nickel containing marked gradients in grain size, ranging from ~30 nm to ~4 μm. Specifically, cracks are grown in a gradient structured (GS) nickel with grain-size gradient ranging from the coarse macro-scale to nano-scale (CG→NG) and *vice versa* (NG→CG), with the measured crack-resistance *R*-curves compared to the corresponding behaviors in uniform nano-grained (NG) and coarse-grained (CG) materials. It is found that the gradient structures display a much-improved combination of high strength and toughness compared to uniform grain-sized materials. However, based on *J*-integral measurements in the gradient materials, the crack-initiation toughness is far higher for cracks grown in the direction of the coarse-to-nano grained gradient than *vice versa*, a result which we ascribe primarily to excessive crack-tip blunting in the coarse-grained microstructure. Both gradient structures, however, display marked rising *R*-curve behavior with exceptional crack-growth toughnesses exceeding 200 MPa.m$^{½}$.

*Keywords: Gradient structural materials; nickel; grain-size gradients; fracture toughness; fracture mechanisms*

## Introduction

A long-standing endeavor for materials scientists is to seek ways to enhance the mechanical properties of engineering structural materials. This effort has led to the notion of "learning from Nature" by studying the structure-property relations in natural materials. Favorable combinations of mechanical properties, including stiffness, strength, and toughness, have been found in natural and biological materials, due to their unique hierarchical structures [1–8]. However, an additional strategy that Nature employs to enhance mechanical properties is through the generation of gradients, in structure, composition, morphology and/or properties [3,9]. For example, bamboo stems possess a gradient structure that comprises a decreasing density

of vascular bundles from their exterior inwards the center, leading to enhanced flexibility yet overall strength and stiffness [10–13]. Crustacean exoskeletons in lobster and crab shells exhibit a gradient transition from fine to coarse Bouligand structures from the outer to inner layers, which results in a hard and stiff outer shell, to resist penetration from predator attacks, with more ductile and tough inner layers to accommodate any excessive deformation [14–16].

Using the inspiration of such natural materials, there have now been several attempts to replicate these gradient structures to create structural metallic materials with similarly favorable combinations of properties. Recent successes have been reported in the fabrication of gradient structured (GS) metals [17–29], such as gradient nano-grained Cu [17,26,28], GS interstitial free steel [22], GS nickel [18,23], gradient nano-twinned Cu [24], gradient nano-twinned steel [19], and gradient nanoscale austenitic/martensitic steels [30,31]. These gradient metallic materials exhibit improved mechanical performance through optimized combinations of strength and ductility [17,19–24], enhanced work hardening [21,22,24], improved fatigue resistance [25–27,32], and excellent wear resistance [28,29], although their fracture toughness has never been investigated. With reference to structural materials, the attainment of strength and ductility is particularly important as these properties are often mutually exclusive. However, a desirable combination of strength and ductility is eminently feasible using the concept of gradient microstructures. Because dislocation activity induced by the incompatible deformation along the gradient can promote strain hardening, which acts both to harden the material while concomitantly delaying the onset of the necking instability to increase the uniform ductility [9,22,33].

While achieving optimized strength and ductility is attractive, the vast majority of structural materials must further display acceptable fracture resistance (or damage tolerance) to avoid catastrophic failure. As resistance to fracture is generally (but not always) associated with a combination of strength and ductility, the attainment of both strength and toughness in a material also tends to be mutually incompatible, yet is critical for most safety-critical applications [34,35]. However, there is a subtilty here; strength and ductility are *global* mechanical responses governed by the deformation of a bulk material volume, whereas the fracture toughness measures the resistance to the initiation or propagation of a crack which actually "samples" the *local* microstructure. For example, the volume of material actively involved in the measurement of strength and ductility pertains typically to the volume of the uniaxial tensile specimen used, but this is many orders of magnitude larger than the process (or plastic) zone corresponding to the active volume of material sampled at the tip of a propagating crack.[1] Therefore, although

[1] This distinction is particularly potent in graded structures as properties like strength, ductility, and the work of fracture (plastic work density) measure these properties integrated over a large volume, whereas stress-intensity or *J*-based resistance curves sample the local structure as the crack propagates throughout the microstructure.

excellent combinations of strength and ductility can be achieved with gradient structures, it does not necessarily guarantee that the fracture resistance will be similarly superior, as the local variance in microstructure, which is inherent in GS materials, may lead to a significant discrepancy in crack resistance. Accordingly, the objective of the present study is to explicitly examine this issue; as gradient materials will possess inherent inhomogeneities in microstructure, we examine how this can specifically affect the resistance to the initiation and propagation of cracks in GS materials.

This work outlines a systematic fracture-mechanics-based study to evaluate the fracture toughness of gradient structured (GS) nickel. Specifically, the crack-driving force required to initiate and propagate a pre-existing crack in gradient grain-sized structures in Ni samples, in the direction from coarse (~4 μm) to nano-scale (~30 nm) grain and from nano-scale to coarse grain (termed, respectively, "CG→NG" and "NG→CG"), are evaluated through measurements of the crack-resistance (*R*-) curves, and compared with corresponding fracture behavior in uniform purely coarse-grained ("CG") and purely nano-grained ("NG") Ni microstructures. Micro-mechanisms associated with the interplay between the propagating crack and the local gradient structure are further revealed by *post-mortem* fractographic analysis and *in situ* microscopy. This study seeks not only to develop a mechanistic understanding of the fracture behavior of GS materials, but also may provide practical guidelines for the use of such materials in safety-critical applications.

## Material and methods

*Materials processing and characterization*

A bulk-sized gradient structured (GS) Ni plate with a thickness of 1.4 mm was designed and synthesized by direct-current electrodeposition. The plating bath composition and operating conditions are described elsewhere [23]. With the current density increased from 10 to 100 $mA.cm^{-2}$ and the additive concentration increased from 1 to 6 g/L, the grain size was continuously refined from ~4 μm to ~30 nm along the deposition direction (Fig. 1a). In order to fabricate bulk-sized GS single-edge bend (SE(B)) specimens for fracture toughness measurements, the GS Ni plate was further coated with 1.6 mm-thick layers of monolithic nano-grained (NG) Ni (grain size ~50 nm) on both ends, forming a sandwich plate with a final dimensions of 60 × 30 × 4.6 $mm^3$ (Fig. 1b). For the purpose of comparison, NG and coarse-grained (CG) SE(B) specimens were prepared by replacing the GS layer of the sandwiched plate with uniform grain-sized NG and CG Ni. The grain sizes of the monolithic NG and CG Ni were ~30 nm and ~4 μm, respectively. All the sandwich-structured plates were annealed at 393 K for 12 hr to relax the residual stress induced by electrodeposition, before machining the SE(B) specimens for fracture toughness measurements.

Microstructures were characterized in the 1.4-mm wide gradient or monolithic ligament in the SE(B) specimens (Fig. 1c) using scanning electron microscopy (SEM) on a Zeiss Supra 55 microscope operating at a voltage of 20 kV in the back-scattered electron (BSE) imaging mode. To obtain the grain-size distributions along the gradient and uniform grain-sized ligaments, we characterized the hardness profile along the deposition direction. This hardness profile was measured using a Qnes Q10 A+ microhardness testing machine with a Vickers indenter. The indentation peak load was 10 g with a dwell time of 10 s. Grain sizes were calculated from the microhardness values using the Hall-Petch relationship as follows:

$$HV = 1.9346 + 16.79d^{-1/2}, \quad (1)$$

where $HV$ is the microhardness value; $d$ represents the grain size. The validation of determining the grain-size distribution from the hardness profile by using Eq. (1) was checked with direct measurements by x-ray diffraction (XRD) and SEM imaging (for further information, see Fig. A.1 in the Supplementary Data). Grain sizes below 1 μm, which were measured by XRD methods, were further verified by transmission electron microscopy (TEM) characterization (see Fig. 5 in [23]).

*Mechanical characterization*

In order to compare the strength and fracture toughness relationship, the same gradient structured sample but with a thickness of 500 μm was prepared for uniaxial tension experiment. Dog-bone shaped rectangular specimens with a gauge cross-section of 0.5 × 1.2 mm$^2$ and a gauge length of 6 mm were machined from the gradient and monolithic Ni plates using electrical discharge machining (EDM). The loading direction of all the tensile specimens was aligned perpendicular to the deposition direction. Before uniaxial tension testing, the dog-bone shaped specimens were electropolished to acquire a smooth and residual-stress-free surface. A laser extensometer was used to measure the engineering strain within the gauge section during loading. Tensile tests were performed at room temperature on an Instron 5848 screw-driven mechanical testing machine (Instron Corporation, Norwood, MA, USA) at an engineering strain rate of 3.0 × $10^{-4}$ s$^{-1}$. At least three tensile specimens for each gradient/monolithic structure were tested to evaluate the statistical significance of the tensile properties.

The yield strength, $\sigma_y$, ultimate tensile strength, $\sigma_{uts}$, and elongation to failure, $\varepsilon_f$, were calculated from the tensile engineering stress-strain curves; their average values and the standard deviations are summarized in Table 1. True stress-strain curves were also calculated in order to extract the plastic work density (*i.e.*, the work of fracture), $u_f = \int_0^{\varepsilon_{f,p}} \sigma d\varepsilon_p$, during tensile fracture; this was determined from the area under the true stress-plastic strain curve, where $\varepsilon_{f,p}$ is the plastic strain corresponding to the elongation to failure, $\varepsilon_f$.

To evaluate the fracture toughness properties, SE(B) specimens, with a thickness of $B$ = 2 mm, width of $W$ = 4 mm and total length of 24 mm, were fabricated from the GS and uniform grain-sized sandwich plate by EDM. To elucidate the influence of gradient orientation on the fracture toughness, two sets of GS specimens, *i.e.*, gradient CG→NG (where cracking initiates in the CG zone and propagates through the gradient CG→NG zone into the NG zone) and gradient NG→ CG (cracking initiates in the NG zone and propagates through the gradient NG→CG zone into the CG zone), were fabricated. The CG→NG and NG→CG specimens were extracted from the same sandwich GS plate to ensure consistency of the grain-size distribution profile (Fig. 1b). For comparison, the NG and CG SE(B) specimens were also fabricated from the uniform grain-sized NG and CG sandwich plates, respectively. Notches, 1.4 mm in depth with a root radius of ~100 μm, were cut in all SE(B) specimens. All specimen surfaces were mechanically polished to 1-μm mirror finish before testing.

Fracture toughness tests were performed in accordance with ASTM Standard E1820 [36]. Prior to testing, the SE(B) specimens were fatigue pre-cracked, to a crack length to width $a/W$ ratio of ~0.45, using a 2.5 kN electro-servo hydraulic MTS load frame (MTS Corporation, Eden Prairie, MN, USA), operating under load control at a stress-intensity range $\Delta K$ of ~8-11 MPa.m$^{1/2}$ at 10 Hz frequency with a load ratio (minimum and maximum applied load) of $R$ = 0.1. To improve the constraint condition at the crack tip, the SE(B) specimens were side-grooved to a depth of 0.2 mm along the crack propagation path using EDM. The side-grooves resulted in a net specimen thickness of $B_N$ of 1.6 mm, such that the total thickness reduction did not exceed 0.25$B$, as recommended by the E1820 Standard [36].

Nonlinear elastic-fracture mechanics[2] involving $R$-curve measurements, characterized in terms of the $J$-integral as a function of crack growth, were used to evaluate the fracture toughness of the GS Ni. Specifically, SE(B) specimens were tested in three-point bending, with a loading span of $S$ =16 mm, under displacement control at a constant displacement rate of 0.1 mm/min. Crack growth was determined by a "multiple-specimen" technique, with individual specimens loaded up to a desired load-line displacement (LLD) prior to being completely unloaded. To determine the physical crack extension corresponding to the specific LLD, the crack length in the

[2] The $J$-integral, like other characterizing parameters in fracture mechanics such as the stress intensity factor $K$, were derived for homogeneous isotropic continua [35]. However, they have been widely used, indeed mostly used, to examine materials and microstructures where such homogeneity is difficult to rationalize. The underlying justification for using such fracture mechanics analyses is that the structural size-scales remain small compared to the extent of the $J$-dominated (or $K$-dominated) crack-tip stress and displacement fields, and that this in turn remains small compared to the macroscale of the test sample.

unloaded specimen was measured using scanning electron microscopy (SEM, Zeiss Supra 55) and a three-dimensional (3D) measuring laser microscope (LEXT OLS4000). By testing multiple specimens interrupted at incremental LLDs, the extent of subcritical crack growth in each sample could be determined in order to derive the *J*-R($\Delta a$) curves for each microstructural test condition.

To establish the *R*-curve, the *J*-integral corresponding to the specific crack extension measured from each specimen was calculated as the sum of elastic $J_e$ and plastic $J_{pl}$ components of $J$:

$$J = J_e + J_{pl} = K^2/E' + J_{pl} \quad , \tag{2}$$

where $E' = E$ (Young's modulus) in plane stress or $E/(1-\nu^2)$ in plane strain ($\nu$ is Poisson's ratio). For pure Ni, $E$ and $\nu$ are 200 GPa and 0.312, respectively. The linear elastic stress intensity $K$ was defined for SE(B) specimen from [36]:

$$K = \frac{PS}{(BB_N)^{1/2}W^{3/2}} \cdot f\left(\frac{a}{W}\right), \tag{3}$$

$$f\left(\frac{a}{W}\right) = 3\sqrt{\frac{a}{W}} \cdot \frac{1.99-\left(\frac{a}{W}\right)\left(1-\frac{a}{W}\right)\left[2.15-3.93\frac{a}{W}+2.7\left(\frac{a}{W}\right)^2\right]}{2\left(1+2\frac{a}{W}\right)\left(1-\frac{a}{W}\right)^{3/2}} \quad , \tag{4}$$

where $P$ is the applied load prior to the complete unloading, $B$ and $B_N$ are the specimen thickness and the net side-grooved thickness, respectively, and $a$ is the initial crack length $a_0$. The plastic component of $J$ is calculated from [36]:

$$J_{pl} = \frac{\eta_{pl}A_{pl}}{B_N b_0} \quad , \tag{5}$$

where $A_{pl}$ is the plastic area under the force vs. the load-line displacement curve, $\eta_{pl}$ is 1.9 if the load-line displacement is used for $A_{pl}$, and $b_0$ is the initial ligament length. The *J*-integral value calculated from Eqs. (2-5) should be corrected for crack growth using the following relationship [37]:

$$J = J_e + \frac{J_{pl}}{1+\left(\frac{\alpha-0.5}{\alpha+0.5}\right)\frac{\Delta a}{b_0}} \quad , \tag{6}$$

where $J_e$ and $J_{pl}$ are determined from Eqs. (2) and (5) with $a_0$ and $b_0$, respectively. $\alpha$ is 1 for SE(B) specimen geometry. $\Delta a = a - a_0$ represents the crack extension, which can be measured as the difference of the crack length $a$ at the specific LLD and the initial crack length $a_0$ after fatigue pre-cracking. Using Eqs. (2) to (5), we can construct the *J*-R($\Delta a$) curve by calculating the *J*-integral corresponding to the specific crack extensions measured from multiple specimens that were unloaded at incremental LLDs.

The provisional toughness $J_Q$ was determined as the intersection of the *R*-curve and the 0.2 mm offset/blunting line with a slope of $2\sigma_0$, where $\sigma_0 = ½(\sigma_y + \sigma_{uts})$ is the flow stress (now

referred to as the effective yield strength in ASTM Standard 1820) as the average value of the yield strength and the ultimate strength. For $J_Q$ to be considered as a size-independent fracture toughness ($J_{Ic}$) value, the validity requirements for the *J*-field dominance and plane-strain conditions should be met, *i.e.*, that $b_0, B > 10J_Q/\sigma_0$, where the $b_0$ and $B$ are the initial ligament length and specimen thickness, respectively. Corresponding *K*-based fracture toughness values were then computed used the standard mode I *J-K* equivalence relationship, $K_{JIc} = (E' J_{Ic})^{½}$ .

*Fractographic characterization*

Fractographic analysis was performed to characterize the failure mechanisms involved in the crack propagation in the GS, NG and CG materials. Featured regions along the crack propagation direction on the fracture surfaces were characterized using a JSM-7500F scanning electron microscopy (JEOL USA, Arvada, CO, USA) operating in the secondary electron imaging mode at 5-15 kV. In addition, the three-dimensional morphology of the fracture surfaces for each grain structured specimen was reconstructed using a KEYENCE 3D Digital Microscope VHX-5000 (Keyence USA, Itasca, IL, USA).

To illuminate the deformation mechanisms in the vicinity of the crack tip, smaller SE(B) specimens, with *W*, *S* and *B* dimensions of 4 × 15 × 1.5 $mm^3$, were prepared and tested in three-point bending (in displacement control) using an *in situ* Gatan MicroTest 2kN bending stage mounted in an Hitachi S-4300SE/N (Hitachi America, Pleasanton, CA, USA) SEM, to observe how the advancing crack interacts with the local microstructural features in real time. These specimens were also fatigue pre-cracked, with specimen surfaces prepared using the same procedures described above for the larger SE(B) specimens; they were characterized *in situ* under load in both the back-scattered and secondary electron imaging modes. To clarify the deformation modes in the coarse-grained zone, electron back-scatter diffraction (EBSD) scans were performed in the vicinity of the blunted crack tip using the FEI Strata DB235 SEM operated at 20 kV using a TEAM™ EBSD analysis system (Ametek EDAX, Mahwah, NJ, USA) with a step size of 50 nm.

To specifically examine the crack-path profile and discern the deformation mechanisms in the vicinity of the crack tip and wake under plane-strain conditions, some SE(B) specimens were interrupted during the fracture toughness testing and sliced through the thickness into two halves at the mid-section thickness. The interior surface of one half was progressively polished to a 0.05-μm surface finish followed by a final vibration polishing using 0.05-μm colloidal silica. The microstructure along the crack wake and the crack-tip region was imaged using back-scattered electrons in the Hitachi S-4300SE/N SEM operating at 10 kV.

## Results

*Microstructures*

SEM images taken from the crack-propagation region in the gradient Ni CG→NG and NG→ CG fracture toughness specimens reveal grain-size gradients with a smooth transition from, respectively, coarse grains to nano-grains and nano-grains to coarse grains, as shown in Figs. 1c,d. Detailed SEM imaging of the coarse-grained region and TEM imaging of the nano-grained region on the gradient structure are illustrated in Fig. A.2. The uniform coarse-grained region contains columnar crystal grains with a size of ~30 μm in the crack-propagation direction (*i.e.*, the electrodeposition direction) and ~4 μm in the transverse direction. The uniform nano-grained region is composed of equiaxed grains with a mean size of ~30 nm. For comparison, pure NG and pure CG fracture toughness specimens with, respectively, completely uniform nano-grains and coarse grains along their crack propagation ligaments are also shown in Figs. 1c,d.

The grain-size profiles were characterized along the crack-propagation ligaments of these gradient Ni fracture toughness specimens; the measured grain size continuously decreases from ~4 μm to ~30 nm in the CG→NG specimen, whereas it increases from ~30 nm to ~4 μm in the NG →CG specimen (Fig. 1e). Specifically, the grain sizes within the initial and final 400-μm regions of these profiles remain constant, indicating that there is a uniform grain size at the beginning and end of each grain-size gradient. The grain-size profiles of CG→NG and NG→CG specimens are completely symmetrical, establishing that the grain-size distributions are identical but in the opposite gradient direction with respect to the progress of crack propagation. The maximum and minimum grain sizes in the two GS specimens are also consistent with the uniform grain sizes in the monolithic CG and NG specimens.

*Strength and ductility*

The engineering stress-strain curves for the pure NG, pure CG, and GS (both CG→NG and NG→CG) structures were measured from dog-bone shaped rectangular specimens subjected to quasi-static uniaxial tension at room temperature (Fig. 2a). Results, listed in Table 1, show that the yield strength decreases from 1095 MPa in NG material, to 687 MPa in GS materials, and to 383 MPa in CG material. Similarly, the ultimate tensile strength of the NG material is 1437 MPa; it is 24% lower in the GS specimen (at 1094 MPa) and 59% lower in CG specimen (at 592 MPa). In contrast to the strength, the total elongation of the NG material is 6.6%; it is 67% higher (at 11 %) in the GS material and almost a factor of 2.2 higher (at 14.2%) in the CG material.

The results from NG and CG samples clearly show a trade-off between strength and ductility, *i.e.*, that the increase in the strength is achieved at the expense of reduced ductility. The tensile strength of the nano-grained NG material is much higher, by almost 2.5 times, than that of the coarse-grained CG material, whereas its ductility is a factor of 2.2 lower. However, a sound

combination of strength and ductility is obtained in the GS Ni materials, consistent with other gradient- and heterogeneous- structured materials [17,19–24]. Such an optimized combination of strength and ductility can be confirmed from an increase in the plastic work density (or work of fracture), *i.e.*, the area under the true stress-plastic strain curve, which is increased from 78.97 $MJ.m^{-3}$ and 72.35 $MJ.m^{-3}$, respectively, in uniform CG and NG specimens to 103.39 $MJ.m^{-3}$ in GS specimens.

*Crack-resistance curves and fracture toughness*

To evaluate the fracture resistance of the gradient- and monolithic- structured Ni, we measured *J*-integral based *R*-curves, *i.e.*, *J* as a function of the stable crack extension, $\Delta a$. The *J*-*R*($\Delta a$) curves for the gradient structured (CG→NG and NG→CG) Ni and the uniform grain-sized (CG and NG) Ni are summarized in Fig. 2b. We used a power-law relationship to fit the experimental *J*-*R*($\Delta a$) curve: $J = C_1(\Delta a)^{C_2}$, where $C_1$ is a scaling constant and $C_2$ is a hardening exponent, in accordance with ASTM Standard E1820 [36]. The parameters $C_1$ and $C_2$ that characterize the hardening behavior of the *J*-*R*($\Delta a$) curves for all specimens are summarized in Table 1.

Rising *R*-curve behavior is seen in all microstructural conditions, although with marked differences in the degree of toughening. For the uniform grain-sized structures, the coarse-grained CG structure displays a far higher crack-growth toughness than the NG structure; to sustain a crack extension of $\Delta a$ ~ 1 mm, the value of the crack-driving force *J* has to be increased to 442.5 $kJ.m^{-2}$ in the CG material, whereas *J* needs only to be increased to 66.3 $kJ.m^{-2}$ to achieve the same crack extension in the NG sample.[3] Indeed, these CG *vs*. NG Ni structures signify quite a distinct mechanical response which, for want of a better term, we can call "ductile" *vs*. "brittle" fracture behavior[4].

In contrast to the relatively low fracture resistance of the NG specimen, the gradient NG→CG specimen presents much enhanced fracture resistance with crack extension. As can be seen in Fig.

[3] According to ASTM Standard 1820, the allowable crack extension should not be larger than $0.25b_o$, where $b_o$ is the original ligament length ($b_o$ ~ 2.2 mm). As a crack extension of 1 mm, where the crack-growth toughness was measured, is beyond the maximum allowable crack extension length of 0.55 mm for our samples, these crack-growth toughness values are not strictly ASTM valid. However, we have used a measurement at $\Delta a$ = 1 mm to represent the total toughening effect as a consequence of the interaction of the growing crack with the local microstructure over the entire length of the gradient.

[4] As nickel has a face-centered cubic structure, it would not normally experience a ductile-to-brittle transition with a brittle fracture mechanism such as cleavage fracture, as is common in body-centered cubic materials, such as ferritic iron. Nickel tends to fail by microvoid coalescence at both low and high temperatures. Accordingly, the term "brittle" is used here, not with reference to a fracture mechanism *per se*, but rather to a low-energy fracture showing little evidence, at the scale of observation, of incumbent plastic deformation, and which is characterized by a low fracture toughness.

2b, the initial slope of the *J-R*(Δ*a*) curve of the NG specimen remains almost constant. By comparison, the corresponding slope of the *R*-curve of the NG→CG specimen increases gradually as the crack extends, especially in the gradient NG→CG zone (0.2 mm < Δ*a* < 0.8 mm), where the fine nano-sized grains progressively transform into coarse micrometer-sized grains. The gradient NG→CG microstructure clearly represents a marked improvement in the toughness and general fracture resistance of the nano-grained nickel material, representing far more ductile behavior.

Unlike the considerable enhancement in the fracture resistance of the gradient NG→CG specimen as compared to that of the uniform NG specimen, there is a much smaller, almost minimal, improvement in the fracture resistance of the gradient CG→NG specimen compared to the CG counterpart. As illustrated in Fig. 2b, the initial portion of the *R*-curve in the CG and CG→NG specimens appears to be essentially the same for crack extensions less than ~0.2 mm where the propagating crack is only encountering coarse grains (Figs. 1d,e). Once the crack extends into the gradient CG→NG zone, the *J*-integral values first increase slightly, by ~17% at Δ*a* ~ 0.3 mm, but only for limited further crack extensions up to ~0.33 mm, followed by rapid unstable crack propagation, as indicated by the dashed red arrow in Fig. 2b. This sharp transition for crack growth in the coarse *vs*. the nano grains again indicates a conversion in fracture mechanisms from ductile (stable crack growth) to brittle (catastrophic fracture) behavior.

Fracture toughness values were calculated from the critical value of *J* at crack initiation, *i.e*., at the intersection of the *R*-curve with the offset/blunting line and then back-calculated to a stress intensity using the *J-K* equivalence. As listed in Table 1, the crack-initiation fracture toughness of the gradient NG→CG material is 86 MPa.m$^{½}$, which is ~59% higher that the toughness of 54 MPa.m$^{½}$ of the uniform nano-grain (NG) material. These values satisfy the ASTM requirements for *J*-dominance at the crack tip and plane-strain conditions [36], and thus represent valid $K_{JIc}$ values. The corresponding fracture toughness value for the gradient CG→NG material is more than a factor of three higher at 274 MPa.m$^{½}$, which is some 7% lower than that of the uniform coarse-grained (CG) material, 296 MPa.m$^{½}$, although these latter values are not strictly ASTM valid [36].

*Fractography*

To discern the active failure mechanisms, fracture surfaces and crack-path profiles were examined for CG, NG, CG→NG, and NG→CG microstructures after toughness testing (Fig. 3). As shown in Fig. 3a, the fracture surface in the CG specimen exhibits typical ductile fracture – following a pronounced stretch zone due to crack-tip blunting (region A), crack initiation and growth by microvoid coalescence (region B). Tearing features are visible on the stretch zone, which likely result from slip-band shear emanating from the crack tip at ~45 deg to the maximum

principal stress; this is also consistent with the pronounced shear lips at the surface edges of the fracture surface. Microvoids observed on the fracture surface are mostly located at triple joints, indicating that the stress concentrations there are the driving force for the initiation of the voids; indeed, the average size of the ductile dimples of ~4 μm matches the size of columnar crystal grains in the transverse direction.

Unlike fractures in the CG specimens, the NG fracture surfaces are macroscopically flat with "dividing" ridges forming river patterns along the crack-propagation direction (Fig. 3b). At crack initiation, the surfaces are "brittle" - almost cleavage-like - with narrow polygon shapes that are stretched along this same direction (region A). With crack extension, larger surfaces are formed progressively, oriented more or less perpendicular to the maximum principal stress direction. Closer examination (region B) reveals that the macroscopically flat surfaces are actually comprised of the coalescence of nano-scale dimples, which have dimensions comparable to the size of the nano-grains (~40 nm), *i.e.*, "brittle-like" fracture caused by conjoining successive micro-dimples nucleated through highly localized plastic tearing within the nano-grains.

Distinct from cracking in the uniform-grained CG or NG microstructures, where respectively ductile and brittle-like fractures ensue, a mixture of both ductile and brittle-like fractographic features are present in the gradient CG→NG and NG→CG structures (Figs. 3c,d). At crack initiation for the CG→NG structure (Fig. 3c), a ductile stretch zone (from the blunting of the pre-crack) is formed (Region A) with crack growth extending from the pure CG region before terminating inside the gradient CG→NG zone. As the crack encounters the gradient microstructure and progressively the nano-grained region, brittle-like fracture surfaces composed of nano- and micro-sized dimples are visible; specifically, when the crack is within the initial portion of the gradient CG→NG zone, some ~50 μm away from the end of the stretch zone, these dimples show a mixture of large (~4 μm) and fine (~40 nm) sizes (Region C). As the crack progresses further, *i.e.*, ~200 μm away from the end of the stretch zone (Region B), dimples with much reduced sizes, ~40 nm and ~1 μm, are apparent, indicating that this region is located near the end of the gradient CG→NG zone. Once within the NG region, the remaining fracture display brittle-like features with flat surfaces composed of nano-scale dimples, only now with large macroscopic shear lips (reflecting plane-stress conditions near the sample surface).

Akin to the CG→NG microstructure, the gradient NG→CG fracture surface displays a similar mix of ductile and brittle features but naturally arranged in a reverse sequence (Fig. 3d). Since crack initiates from pre-crack within the pure NG zone, the initial part of the fracture surface show brittle features, *i.e.*, a region of flat fracture, perpendicular to the principal stress direction, and two shear lips at the surface which become progressively large with crack extension. As with the CG→NG structure, a bimodal distribution of the size of the dimples is again seen; in Region

C, they are sized at ~40 nm and ~1 μm, whereas in Region B, where the crack is closer to the CG portion of the gradient, the sizes are typically a mixture of ~40 nm and ~8 μm. This indicates that the brittle-like fracture mode, that originated from the pure NG zone, continues into the initial part of the gradient NG→CG zone, whereupon there is increasing evidence of the more ductile, coarser void coalescence, mechanism of fracture as the crack leaves the CG→NG zone and grows into the uniform coarse-grained microstructure.

*In situ SEM observation*

To fully understand the crack-resistance behavior, it is revealing to image in real time how the propagating crack interacts with the local grain structures. To achieve this, small SE(B) specimens were tested *in situ* in three-point bending in the SEM (procedures are described in the Methods section). The evolution of the deformation modes during crack propagation in the uniformed-grained CG and NG microstructures are summarized in Figs. 4a-d and 4e-g, respectively. Note that as these are observed at the surface, they reflect both flat (pure mode I) and shear lip modes of crack extension.

For the relatively low strength CG structure, on loading to 275 N, the sharp pre-crack (Fig. 4a) can be seen to initially extend ~2 μm with marked crack opening (Fig. 4b) associated with shear bands emanating from the crack tip into the neighboring grains. At a load of 447 N, where yielding is apparent in the load-displacement curve, the crack becomes severely blunted with a large-scale plastic zone surrounding the crack tip (Fig. 4c). With a continued blunting, the crack extends in a tearing mode, with extensive shear deformation extending as elongated zones from the crack tip (Fig. 4c) with additional multiple shear bands (on {1 1 1} planes) in favorably-oriented coarse grains (for further information, see Supplementary Fig. A.3). It is evident that during the prolonged elastic-plastic deformation following crack initiation, sustained slip-accommodated crack-tip blunting in the coarse-grained structure provides significant fracture resistance (Fig. 2b); this can be seen from the large stretch zone on the fracture surface (Fig. 3a). Once a peak load of 464 N is reached, the load gradually diminishes as an extensive plastic zone is developed ahead of the crack tip. In this region (Region A, Fig. 4d), double and/or multiple {1 1 1} slip bands are again visible in the severely deformed grains. In region B (Fig. 4d), a transition in fracture mode from tearing to mode-I tensile opening is evident with microvoids nucleating at the intersection of multiple slip bands (arrow in Region B). The coalescence of microvoids results in the ductile dimples, which are observed on the fracture surface directly ahead of the stretch zone (Region B, Fig. 3a).

For the much stronger uniform-grained NG specimen, crack initiation occurs at a much lower load of 140 N, with small-scale yielding in the form of two shear bands radiating out from the

crack tip (Fig. 4e). With an increase in load to 170 N, the crack propagates along path directly ahead of the tip approximately perpendicular to the maximum principal stress, with successive microcracks nucleated from nano-grains conjoined ahead of the main crack (Fig. 4f). As indicated by the nano-dimples on the flat fracture surface (Region B in Fig. 3b), these microcracks appear to result from restricted plastic deformation within the nano-grains. At a peak load of 206 N, the load drops quickly during unstable crack advance to a length of ~800 μm. As shown in Fig. 4g, the crack at this point displays both a mode I and shear mode of propagation, reflective of it being imaged at the surface of the test specimen.

For the gradient structures, crack initiation at a load of 430 N occurs in the CG zone of the CG→NG specimen in a tearing mode with the major crack-tip blunting accommodated by dislocation slip (Fig. 5a). At a load of 500 N just prior to the peak load (505 N), the blunted crack tip approaches the edge of the gradient CG→NG zone (Fig. 5b); this is followed by a small reduction of load to 465 N whereupon the load drops precipitously as a brittle crack initiates ahead of the blunted crack tip within the nano-grains near the end of the gradient CG→NG zone (red arrow in Fig. 5c) and propagates into the NG zone. Interestingly, there is a short inclined crack at the initiation end of this larger brittle crack (Region A, Fig. 5c), suggesting that this crack linked with the main crack via with a second branch backward into the gradient CG→NG towards the coarser-grain side. This formation of a brittle crack ahead of a crack tip is akin to the formation of stress-controlled brittle cracks in steels; as the maximum local stresses peak *ahead* of a blunted crack tip, prior to unstable propagation such brittle cracks initiate at a characteristic distance ahead of the tip, which for extreme blunting can reach close the edge of the plastic zone [38,39].

As observed in Fig. 5c, the profuse plastic shear bands originate from the coarse grains and extend into the gradient CG→NG zone, suggesting that the edge of the plastic zone at this point is close to end of the gradient CG→NG zone, which is populated primarily by nano grains. As any stress relaxation by plastic deformation would be suppressed by the much harder nano-grained structure, a stress-controlled brittle crack would be expected to be initiated ahead of the blunted crack in this region, as evidenced in Region A in Fig. 5c. This burst of brittle cracking into the NG region is consistent with the measured *R*-curve behavior (Fig. 2b) where unstable crack propagation occurs when crack grows ~130 μm into the gradient zone. In light of this, it is worth mentioning that the inclined brittle surface next to the stretch zone, where mixed-sized micro-dimples are observed on the fracture surface (Region A, Fig. 3c), is likely produced by crack extension in the opposite direction, *i.e.*, from a crack, initiated ahead of the crack tip, linking back to the main crack.

For the corresponding gradient NG→CG specimen, during initial cracking in the NG zone, propagation occurs, as in the uniform-grained NG specimen (Fig. 3b), as a macroscopically brittle fracture consisting of the coalescence of nano-dimples. Once the maximum load of 354 N is reached, the load drops quickly (Fig. 6d) as the blunted crack extends as two inclined shear branches (Fig. 6a), reflective of intense surface shear lips. Note that at this stage, cracking has not reached the gradient zone. The load then decreases to 239 N and essentially remains constant (Fig. 6d) as one brittle crack proceeds into the gradient NG→CG zone. This is shown in Fig. 6b where severe plastic deformation is evident in the form of pronounced slip bands (see arrows in Region A) that are developed as the crack intrudes into the coarser grains of the gradient. With further loading, the crack essentially arrests due to severe crack-tip blunting in these coarser grains at end of the gradient region (Fig. 6c).

As characterized by the *R*-curve of NG-CG specimen (Fig. 2b), crack resistance is increased when the crack enters into the gradient zone, which can be ascribed to the major toughening effect caused by the "arrest" of the brittle crack from excessive crack-tip blunting due to plastic deformation in the coarser grains. Specifically, the initial straight crack propagation in the NG zone and the initial nano-grained portion of the gradient NG→CG zone results in a brittle (nano-scale void coalescence) fracture, whereas significant crack-tip blunting ensues near the end of gradient zone once the cracks encounters the coarser-grained region, consistent with the large stretch zones seen on the fracture surface (Fig. 3d).

*Crack paths on the mid-plane (plane-strain) cross section*

Although *in situ* SEM studies are invaluable for revealing the fracture mechanisms in terms of how the crack interacts with the microstructure, as the images are of the free surface, the deformation and failure modes pertain to plane-stress conditions. Accordingly, to characterize the corresponding phenomena under plane-strain conditions, test specimens were first loaded to a pertinent point on the *R*-curve, unloaded and sliced through the thickness at mid-section and examined in the SEM using the back-scattered electron mode. Such plane-strain crack-path sections for all four CG, NG, CG→NG and NG→CG microstructures are compared with the surface (plane-stress) profiles in Fig. 7.

Fig. 7a shows the mid-plane crack profile of the CG specimen unloaded from a peak load of 367 N. The process of ductile fracture is clearly observed in the form of a blunted crack tip with the coalescence of microvoids ahead of it, similar to that observed at the specimen surface. For the NG specimen, the crack profile at mid-thickness is also mode-I, *i.e.*, essentially straight and perpendicular to the maximum principal stress direction; the corresponding plane-stress surface profile is curved, *i.e.*, indicative of shear lip formation (Fig. 7b).

For the CG→NG specimen, the mid-plane crack profile shows the major crack blunted in the initial, coarse-grained, region of the gradient CG→NG zone (Fig. 7c). A second brittle crack has initiated in the upper portion of the blunted crack tip, at a location near the nano-grained end of the gradient zone, with two branches following different propagation routes. Consistent with that observed at the free surface during the *in situ* loading, we surmise that one branch, which is parallel to the horizontal line, propagates into the NG zone, while the other branch, which is slightly inclined to the horizontal line, extends in the opposite direction into the gradient zone, to link with the blunted major crack tip. To summarize, fracture in the lower strength, coarse-grained region of the gradient is characterized by significant crack blunting, whereas the initiation of cracking in the much higher strength, nano-grained region of the CG→NG gradient zone is associated by the formation of brittle cracking (from the linking of nano-voids) which appears to nucleate due to the highest triaxial stresses located ahead of the blunted major crack.

For the NG→CG specimen, in plane strain the initial brittle crack aligns with the horizontal line along the mode-I crack propagation direction, whereas the plane stress (free surface) image showing inclined cracking representative of the shear lip (Fig. 7d). With further crack advance into the gradient NG→CG zone, however, major crack-tip blunting and essentially crack arrest occurs as the crack path contacts the coarser-grained region. The steep curvature of the shape of the blunting zone is consistent with the stretch zone shown in Fig. 3d.

## Discussion

We have attempted in this work to demonstrate that by using a gradient structure, comprising gradients in both grain size, ranging from nano-sized (~30 nm) to coarse (~4 μm) grains, and accordingly tensile strength, respectively ranging from ~1400 MPa to ~590 MPa, that an optimized combination of excellent strength (>1 GPa) and tensile ductility (11%) can be achieved at the macro-scale in pure metallic nickel. However, what is particularly impressive is that the gradient structures can display a significantly improved fracture toughness, compared to that of the corresponding uniform grain-sized materials, while retaining such high tensile strength levels. This is shown in Fig. 8 where the fracture toughness of the gradient CG→NG and NG→CG structures are compared with that of the uniformed grain-sized CG and NG structures as a function of ultimate strength. In Fig. 8a, a global measure of the toughness, that of the plastic work density (or work of fracture) measured in a uniaxial tensile specimen, is plotted where this effect is clearly apparent; the toughness of the gradient structures is almost 30% higher than that of the uniform grain-sized materials with a strength level over 80% higher than the lower strength CG material and only 14% lower than the very high strength NG structure. This elevation of fracture work further confirms the enhanced strain hardening capability in the gradient structures where dislocation activity is promoted as a result of incompatible deformation along

the gradient direction. Plotting an alternative measure of toughness, that of the fracture toughness $K_{JIc}$ for crack initiation and the crack growth toughness $K_{ss}$ at $\Delta a$ ~ 1 mm, as functions of the ultimate strength (Figs. 8b, c), we find that this combination of high strength and toughness in the gradient structures is retained, even though the process zone at the crack tip statistically samples a far smaller volume of material (by several orders of magnitude). However, now the toughness, in terms of the *R*-curve crack-growth toughness, is a function of crack direction with respect to the gradient. Specifically, as seen in Fig. 8b, the initiation toughness of the gradient NG→CG structure is some 50% higher than that of the NG structure but with a ~14% lower yield strength, whereas the gradient CG→NG structure exhibits a similar, extremely high, initiation toughness as the CG structure but with almost twice its ultimate strength. More remarkably, the gradient NG→CG structure presents superior crack-growth toughness at $\Delta a$ ~ 1 mm, 87% higher than that in the NG structure, as shown in Fig. 8c. The microstructure-dependent crack resistance in the gradient Ni reinforces the fact that the crack initiation and growth toughness properties result from the interaction of the crack with the local microstructures over small volumes, whereas strength and ductility represent a bulk mechanical response as a consequence of the deformation accommodated by the entire gradient (or inhomogeneous) material volume.

Finally, from the perspective of the application of such gradient nano-/micro-structures as structural materials, resistance to fracture without compromise in strength is clearly a vital requirement, but the fracture resistance must involve *R*-curve behavior; structural materials in practice cannot fracture catastrophically without warning - some degree of stable cracking prior to unstable fracture is essentially mandatory. In this regard, the gradient nickel structures in the present study show very significant rising *R*-curve behavior with marked crack-growth toughness. These crack-growth toughnesses are listed in Table 1 as the *J* and *K* for 1 mm of crack extension; values for the NG→CG and CG→NG gradient structures are, respectively, $K_{ss}$ = 227 and 311 MPa.m$^{½}$, which represent exceptionally high toughness levels. It is noteworthy, however, that although the CG→NG gradient structure has the optimal combination of strength and toughness, unstable cracking can be readily activated once the blunted crack tip approaches the nano-grained end of the gradient zone. Therefore, the NG→CG gradient structure might be preferred for some safety-critical applications, even though its toughness is lower than the CG→NG structure and its strength is lower than uniformed-grained NG structure; this is because provided crack advance is occurring in the NG→CG direction, this gradient structure can "arrest" any initial brittle cracks in the coarser-grained end of the gradient zone and accordingly could provide a more effective resistance to total fracture. In fact, such NG→CG gradient structures are widely utilized in Nature in numerous organisms, such as teeth, fish scales and seashells, where a hard outer surface is required for wear or penetration resistance with graded subsurface layers

of softer, yet tougher, material to maintain the structural integrity of the part by promoting resistance to fracture [14,40,41].

## Conclusions

A systematic study has been carried out to evaluate the deformation and fracture properties of gradient structured (GS) nickel, involving grain size gradients from ~30 nm to 4 μm (NG→CG and CG→NG structures), primarily using nonlinear-elastic fracture mechanics methodologies. The crack resistance and the associated deformation and fracture mechanisms are characterized for the gradient Ni structures through the measurement of uniaxial tensile properties and fracture toughness *R*-curves, and compared with corresponding behavior for uniformed coarse (CG) and nano-scale (NG) grain-sized structures. The major conclusions drawn from this study are as follows:

1. Compared to the ultrahigh-strength NG and low-strength CG uniformed grain-sized structures, an optimized combination of high strength and high toughness can be achieved in the gradient structured material, with the fracture resistance of such GS material dependent on the interaction of propagating cracks with the local microstructure within the gradient.
2. The CG→NG gradient structure, where a pre-existing crack initiates from CG zone and propagates into NG zone, displays the best combination of strength and toughness properties; with largest degree of *R*-curve toughening behavior, similar to the CG material. Once crack extension approaches the end of gradient structure, however, unstable brittle fracture can occur as the crack encounters the nano-sized grains.
3. The NG→CG gradient structure, where a pre-existing crack initiates from NG zone and propagates into CG zone, exhibits a degree of *R*-curve toughening in excess of the NG structure, but less than that of the CG→NG gradient structure. However, it is less susceptible to outright fracture as the propagation of brittle cracks in the nano-grains of the early part of the gradient region become arrested once they reach the coarser-grained regions due to excessive crack-tip blunting. Such crack blunting, which is manifest as a stretch-zone on the fracture surface, represents a particularly potent mechanism of fracture resistance in these metallic nickel structures.

## Data availability

Experimental data from this study are available from Dr. Qin Yu of the Lawrence Berkeley National Laboratory (email: qinyu@lbl.gov) and from Dr. Yi Li from the Institute for Metals Research, Shenyang (email: liyi@imr.ac.cn) upon reasonable request.

## Acknowledgements

This work was supported by the U.S. Department of Energy, Office of Science, Basic Energy Sciences, Materials Sciences and Engineering Division (for Q.Y. and R.O.R) under contract no. DE-AC02-05-CH11231 to the Mechanical Behavior of Materials Program (KC13) at the Lawrence Berkeley National Laboratory (LBNL). Y.L. and J.P. acknowledge financial support from the National Key Research and Development Program of China (No. 2017YFB0702003) and from National Natural Science Foundation of China under Grant No. 51471165. EBSD microscopy was carried out at LBNL's Molecular Foundry supported by the Office of Science, Office of Basic Energy Sciences, of the U.S. Department of Energy under contract no. DE-AC02-05-CH11231.

## Appendix A. Supplementary data

Supplementary data associated with this article can be found in the online version.

## References

[1] R.O. Ritchie, M.J. Buehler, P. Hansma, Phys. Today 62 (2009) 41–47.

[2] U.G.K. Wegst, H. Bai, E. Saiz, A.P. Tomsia, R.O. Ritchie, Nat. Mater. 14 (2014) 23–36.

[3] Z. Liu, M.A. Meyers, Z. Zhang, R.O. Ritchie, Prog. Mater. Sci. (2017).

[4] A.R. Studart, Adv. Funct. Mater. 23 (2013) 4423–4436.

[5] M.A. Meyers, J. McKittrick, P.-Y. Chen, Science (80-. ). 339 (2013) 773–779.

[6] P.-Y. Chen, J. McKittrick, M.A. Meyers, Prog. Mater. Sci. 57 (2012) 1492–1704.

[7] J.W.C. Dunlop, P. Fratzl, Annu. Rev. Mater. Res. 40 (2010) 1–24.

[8] F. Barthelat, Z. Yin, M.J. Buehler, Nat. Rev. Mater. 1 (2016) 16007.

[9] M.F. Ashby, Philos. Mag. A J. Theor. Exp. Appl. Phys. 21 (1970) 399–424.

[10] S. Amada, Y. Ichikawa, T. Munekata, Y. Nagase, H. Shimizu, Compos. Part B Eng. 28 (1997) 13–20.

[11] M.K. Habibi, A.T. Samaei, B. Gheshlaghi, J. Lu, Y. Lu, Acta Biomater. 16 (2015) 178–186.

[12] T. Tan, N. Rahbar, S.M. Allameh, S. Kwofie, D. Dissmore, K. Ghavami, W.O. Soboyejo, Acta Biomater. 7 (2011) 3796–3803.

[13] H.S. Gupta, W. Wagermaier, G.A. Zickler, D. Raz-Ben Aroush, S.S. Funari, P. Roschger, H.D. Wagner, P. Fratzl, Nano Lett. 5 (2005) 2108–2111.

[14] P.-Y. Chen, A.Y.-M. Lin, J. McKittrick, M.A. Meyers, Acta Biomater. 4 (2008) 587–596.

[15] F. Boßelmann, P. Romano, H. Fabritius, D. Raabe, M. Epple, Thermochim. Acta 463 (2007)

65–68.

[16] D. Raabe, C. Sachs, P. Romano, Acta Mater. 53 (2005) 4281–4292.

[17] T.H. Fang, W.L. Li, N.R. Tao, K. Lu, Science 331 (2011) 1587–90.

[18] X.C. Liu, H.W. Zhang, K. Lu, Science (80-. ). 342 (2013) 337–340.

[19] Y. Wei, Y. Li, L. Zhu, Y. Liu, X. Lei, G. Wang, Y. Wu, Z. Mi, J. Liu, H. Wang, H. Gao, Nat. Commun. 5 (2014) 1–8.

[20] E. Ma, T. Zhu, Mater. Today 20 (2017) 323–331.

[21] X.L. Wu, P. Jiang, L. Chen, J.F. Zhang, F.P. Yuan, Y.T. Zhu, Mater. Res. Lett. 2 (2014) 185–191.

[22] X. Wu, P. Jiang, L. Chen, F. Yuan, Y.T. Zhu, Proc. Natl. Acad. Sci. 111 (2014) 7197–7201.

[23] Y. Lin, J. Pan, H.F. Zhou, H.J. Gao, Y. Li, Acta Mater. 153 (2018) 279–289.

[24] Z. Cheng, H. Zhou, Q. Lu, H. Gao, L. Lu, Science (80-. ). 362 (2018) eaau1925.

[25] T. Roland, D. Retraint, K. Lu, J. Lu, Scr. Mater. 54 (2006) 1949–1954.

[26] L. Yang, N.R. Tao, K. Lu, L. Lu, Scr. Mater. 68 (2013) 801–804.

[27] H.W. Huang, Z.B. Wang, J. Lu, K. Lu, Acta Mater. 87 (2015) 150–160.

[28] X. Chen, Z. Han, X. Li, K. Lu, Sci. Adv. 2 (2016) e1601942.

[29] Z.. Wang, N.. Tao, S. Li, W. Wang, G. Liu, J. Lu, K. Lu, Mater. Sci. Eng. A 352 (2003) 144–149.

[30] S.C. Cao, J. Liu, L. Zhu, L. Li, M. Dao, J. Lu, R.O. Ritchie, Sci. Rep. 8 (2018) 5088.

[31] F. Lefevre-Schlick, O. Bouaziz, Y. Brechet, J.D. Embury, Mater. Sci. Eng. A 491 (2008) 80–87.

[32] R.H.J. Peerlings, W.A.M. Brekelmans, R. de Borst, M.G.D. Geers, Int. J. Numer. Methods Eng. 49 (2000) 1547–1569.

[33] Z. Zeng, X. Li, D. Xu, L. Lu, H. Gao, T. Zhu, Extrem. Mech. Lett. 8 (2016) 213–219.

[34] R.O. Ritchie, Nat. Mater. 10 (2011) 817–22.

[35] R. Pippan, A. Hohenwarter, Mater. Res. Lett. 4 (2016) 127–136.

[36] E08 Committee, E1820-17a Standard Test Method for Measurement of Fracture Toughness (ASTM International, 2017).

[37] K. Wallin, A. Laukkanen, Eng. Fract. Mech. 71 (2004) 1601–1614.

[38] R.O. Ritchie, J.F. Knott, J.R. Rice, J. Mech. Phys. Solids 21 (1973) 395–410.

[39] R.O. Ritchie, A.W. Thompson, Metall. Trans. A 16 (1985) 233–248.

[40] S. Bechtle, S. Habelitz, A. Klocke, T. Fett, G.A. Schneider, Biomaterials 31 (2010) 375–384.

[41] E.D. Yilmaz, G.A. Schneider, M. V. Swain, Philos. Trans. R. Soc. A 373 (2015) 20140130–20140130.

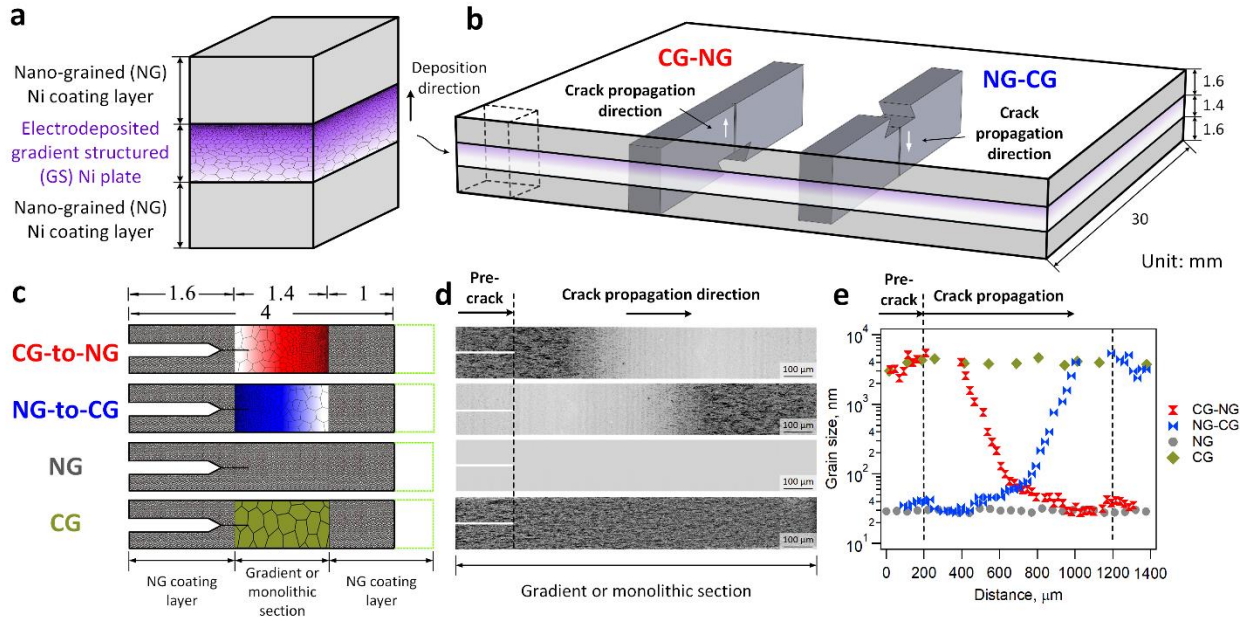


**FIGURE 1** Processing and microstructure of the gradient structured (GS) and uniform grain-sized monolithic structured (MS) nickel. (a) A bulk-sized GS Ni plate with a thickness of 1.4 mm was designed and synthesized by direct current electrodeposition. With increasing the current density and the additive concentration, the grain size continuously refined from ~4 μm to ~ 30 nm along the deposition direction. (b) The GS Ni plate was coated with 1.6 mm-thick layers of monolithic nano-grained (NG) (grain size ~50 nm) on both upper and bottom planes, forming a sandwich plate with final dimensions of 60 × 30 × 4.6 $mm^3$, from which the specimens for uniaxial tensile and fracture toughness tests were machined. (c) To study the crack resistance of gradient structure, pre-cracked single edge bend (SE(B)) specimens were prepared from four grain structures: CG→NG, NG→CG, pure NG, and pure CG. (d) Scanning electron microscopy (SEM) images reveal smooth transitions from coarse grains to nano-grains (or nano-grains to coarse grains) in the gradient ligaments, and uniform coarse (or nano-) grains in MS ligaments. (e) The gradient grain-size distribution in the GS ligaments and the uniform grain-size distribution in the MS ligaments were extracted from the microhardness profiles characterized along the crack-propagation ligaments.

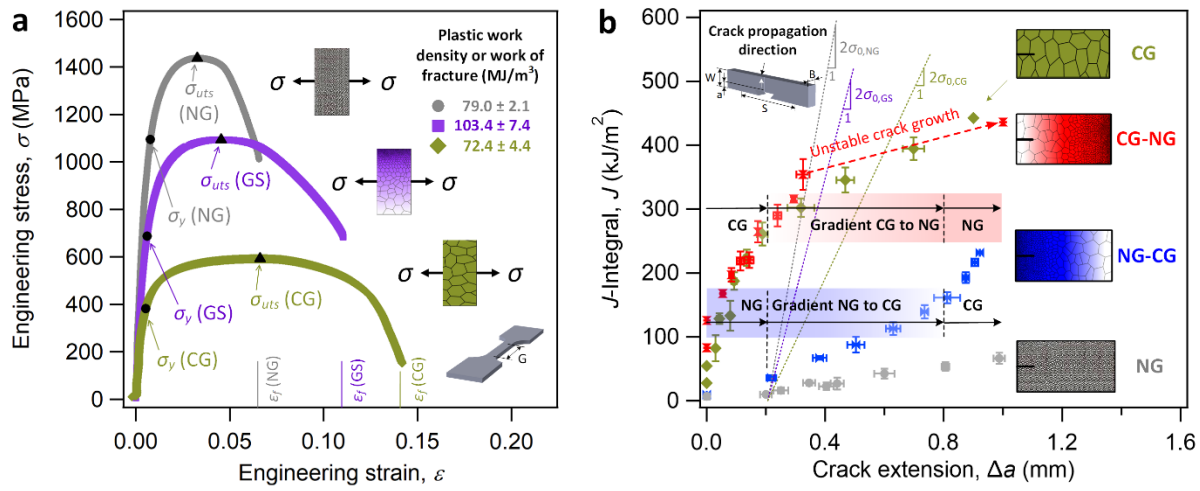


**FIGURE 2** Mechanical properties of the uniform grain-sized pure NG and pure CG structures, and gradient structured (CG→NG and NG→CG) Ni at room temperature. (a) Uniaxial tensile properties of NG specimen show an increase in both yield strength and ultimate tensile strength compared to those in CG specimen. A good combination of strength and ductility can be achieved in the GS specimen as confirmed by the increase of plastic work density (or work of fracture), *i.e.*, the area under the true stress-plastic strain curve, in the GS specimen from those in the CG and NG specimens. (b) *R*-curves for the four structures presented in terms of *J*-integral as a function of crack extension $\Delta a$. As the crack grows to $\Delta a$ = 1 mm, the *J*-integral value of the CG specimen is increased to 442 kJ.m$^{-2}$, some six times higher that of the NG sample, 63 kJ.m$^{-2}$, showing evidence of ductile and brittle crack-growth behavior in the CG and NG structures, respectively. The *R*-curve of the gradient NG→CG materials shows an increasing slope, compared to that of the pure NG structure, as the crack grows into the gradient region, indicating an enhanced crack-growth toughness. The gradient CG→NG specimen presents a similar crack resistance to the CG specimen until crack extension ends in the initial part of the gradient zone, whereupon unstable crack growth occurs into the nano-grained region. A transition in the fracture mode from ductile to "brittle" is apparent as the crack proceeds through the CG→NG gradient in this material.

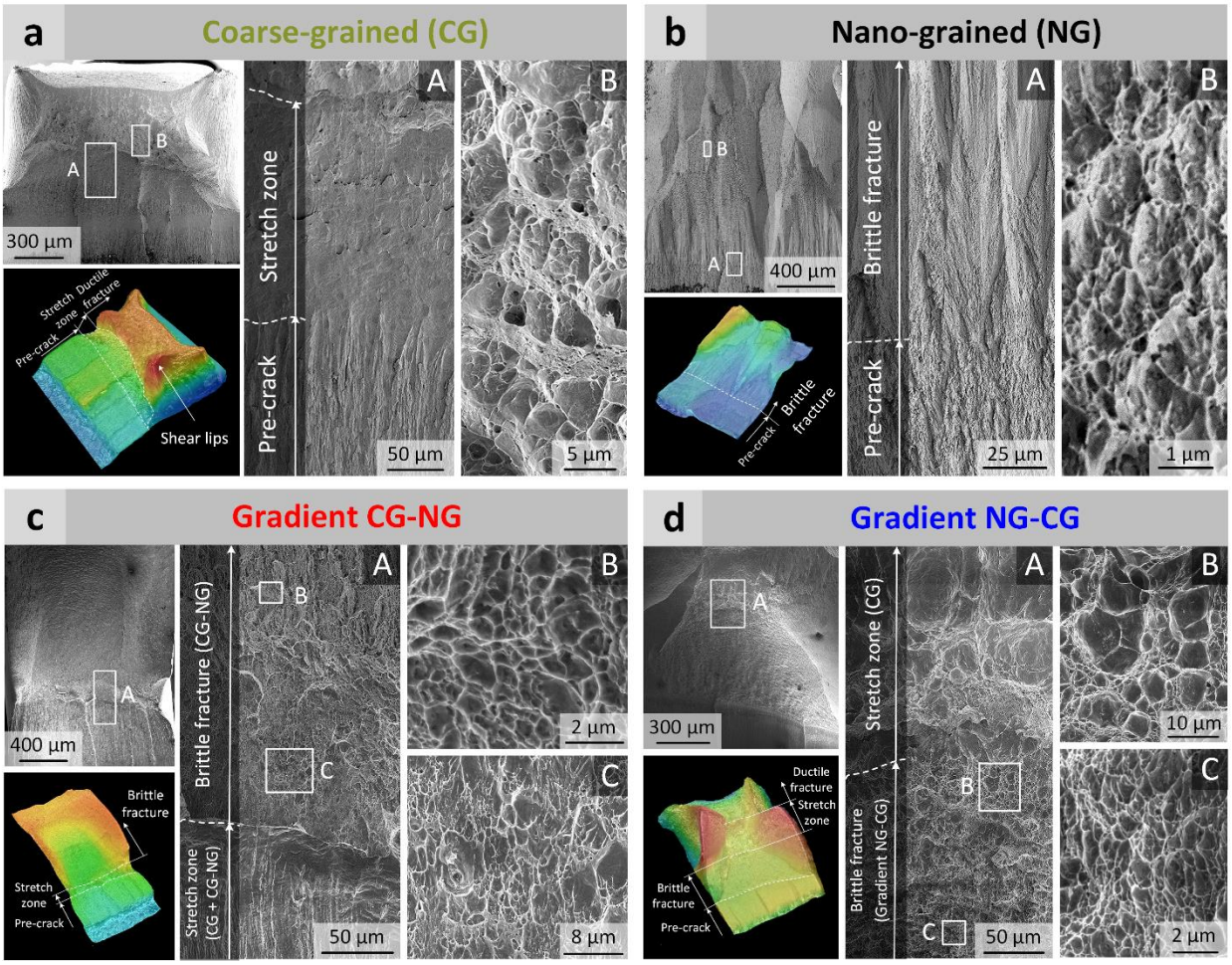


**FIGURE 3** Fractographic features examined on the separated fracture surfaces for the *in situ* SEM tested GS and MS Ni specimens. (a) CG fracture surface shows a transition from the pre-crack to a tearing stretch zone followed by full ductile fracture surface composed by ductile dimples. (b) NG fracture surface shows typical brittle feature in macroscopic appearance, where irregular-shaped flat surfaces are connected at "dividing" ridges, forming "river patterns" along the crack propagation direction. (c) A mixture of ductile and brittle features is shown in CG→NG fracture surface. After a short stretch zone within the CG zone at crack initiation, brittle fracture surfaces are followed in the gradient CG→NG zone and extend further into the NG zone. (d) The NG→CG fracture surface presents a mixture of brittle and ductile features similar to the CG→NG case yet in a reverse order. Brittle fracture surfaces are first formed at crack initiation in the pure NG zone and extend into the gradient NG→CG zone. As crack grows further into the CG zone, pronounced stretch zone and full ductile fracture surfaces are developed.

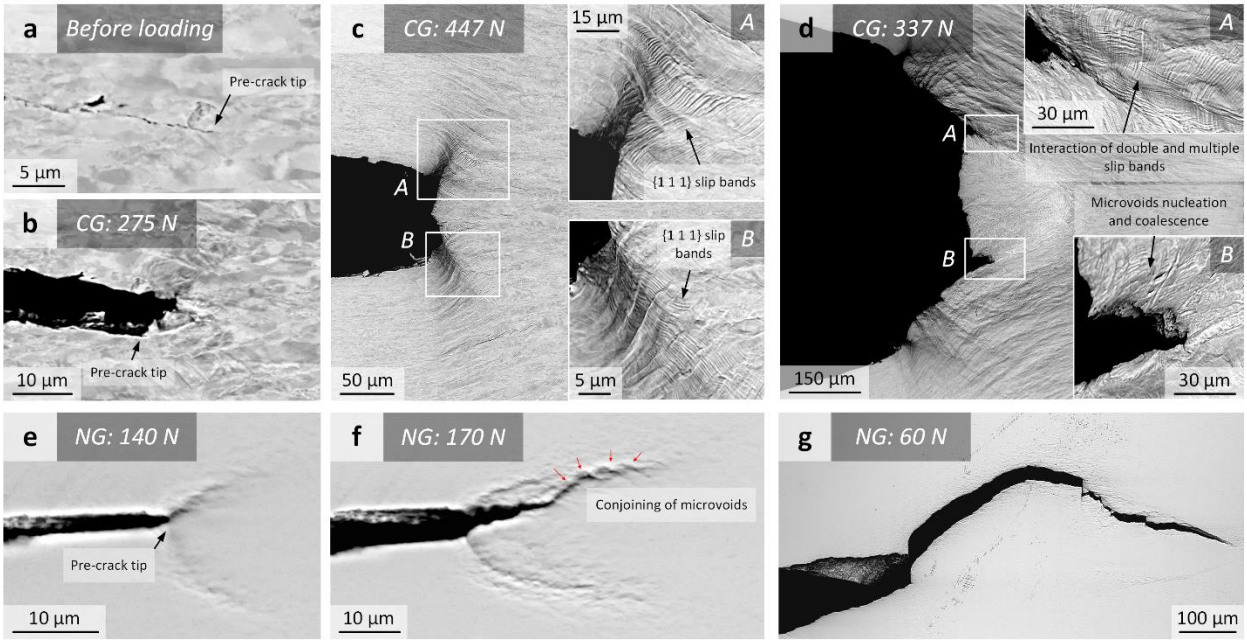


**FIGURE 4** Evolution of the deformation and fracture modes in the crack-tip region for the CG (a-d) and NG (e-g) specimens. *In situ* SEM images of (a) the pre-crack tip in CG specimen before loading. (b) Extensive plastic deformation active at the crack tip at 275 N. (c) At 447 N, pronounced slip bands developed in the shear zones ahead of crack front. (d) Cracking advances by coalescence of microvoids nucleation at intersected slip bands. (e) Crack initiation from the pre-crack at a load of 140 N. (f) Crack propagation through conjoining of microcracks originated from the nano-grains. (g) Full brittle crack profile developed on the NG specimen surface.

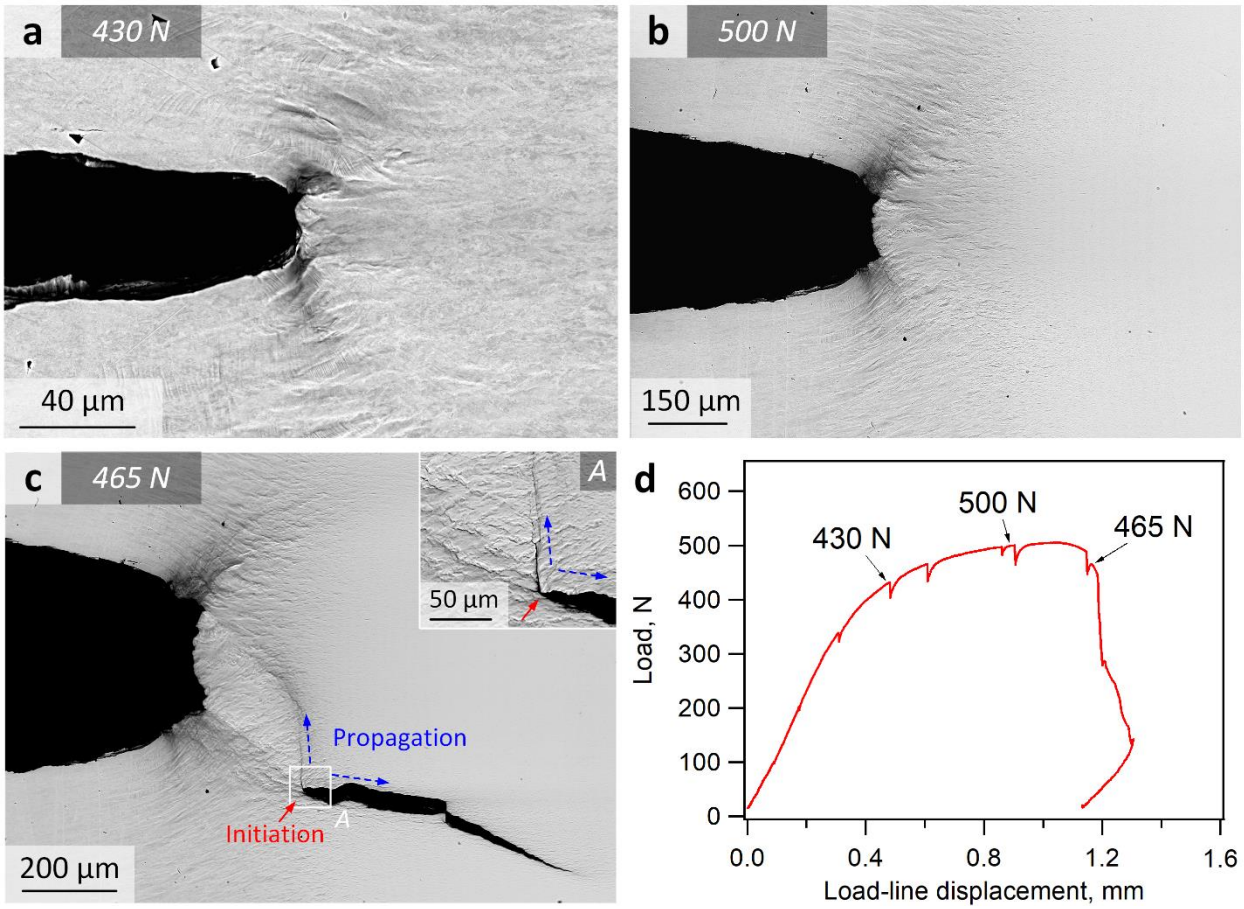


**FIGURE 5** Evolution of the deformation and fracture modes in the crack-tip region for the CG→NG specimen. *In situ* SEM images of (a) crack propagating in the tearing mode with sustained crack-tip blunting in the CG zone. (b) The blunted crack-tip near the peak load of 500 N. (c) At 465 N just exceeding the peak load, a brittle crack initiates away from the main blunted crack tip near the end of the gradient CG→NG zone. (d) The load-displacement curve showing the loading conditions, where the *in situ* images were taken.

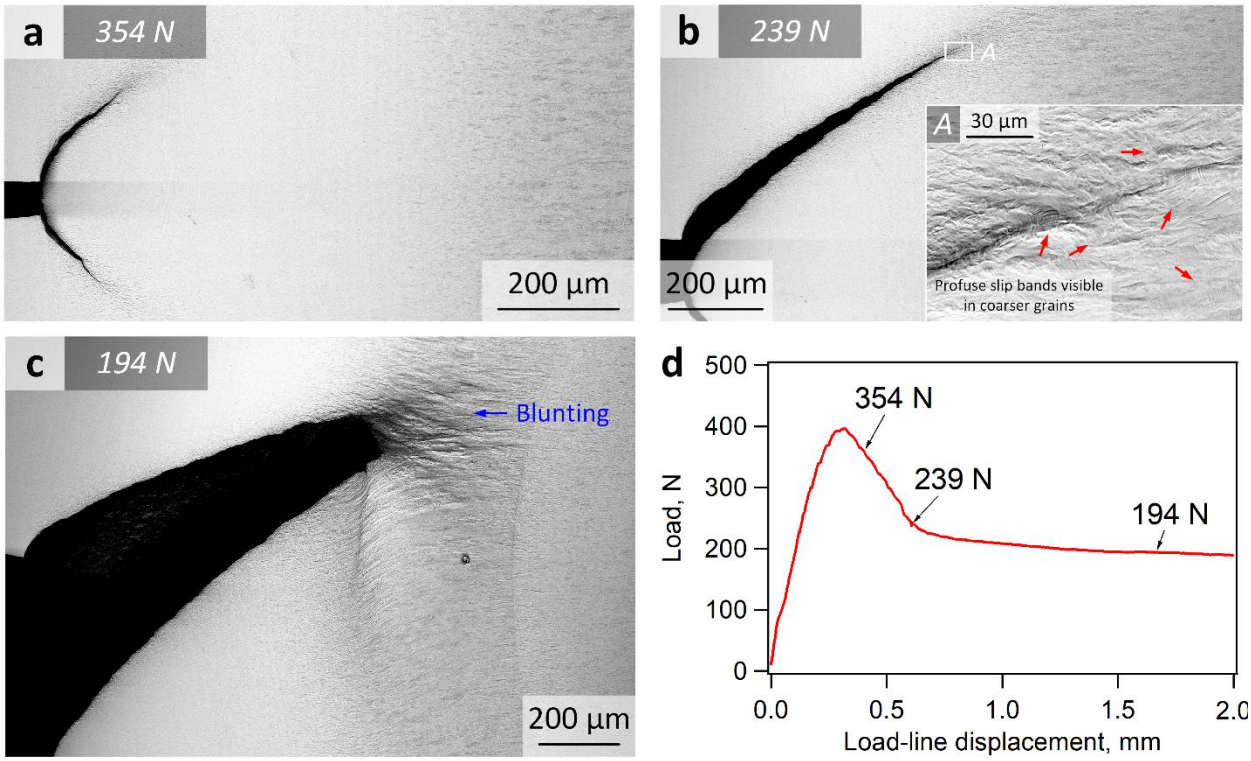


**FIGURE 6** Evolution of the deformation and fracture modes in the crack-tip region for the NG→CG specimen. *In situ* SEM images of (a) brittle crack propagation in the pure NG zone, followed by (b) crack propagation into the gradient NG→CG zone, where pronounced slip bands are visible in the coarser grains (arrows in region *A*). (c) The crack tip becomes blunted within the coarse-grained structure near the end of the gradient NG →CG zone. (d) The load-displacement curve showing the loading conditions, where the *in situ* images were taken.

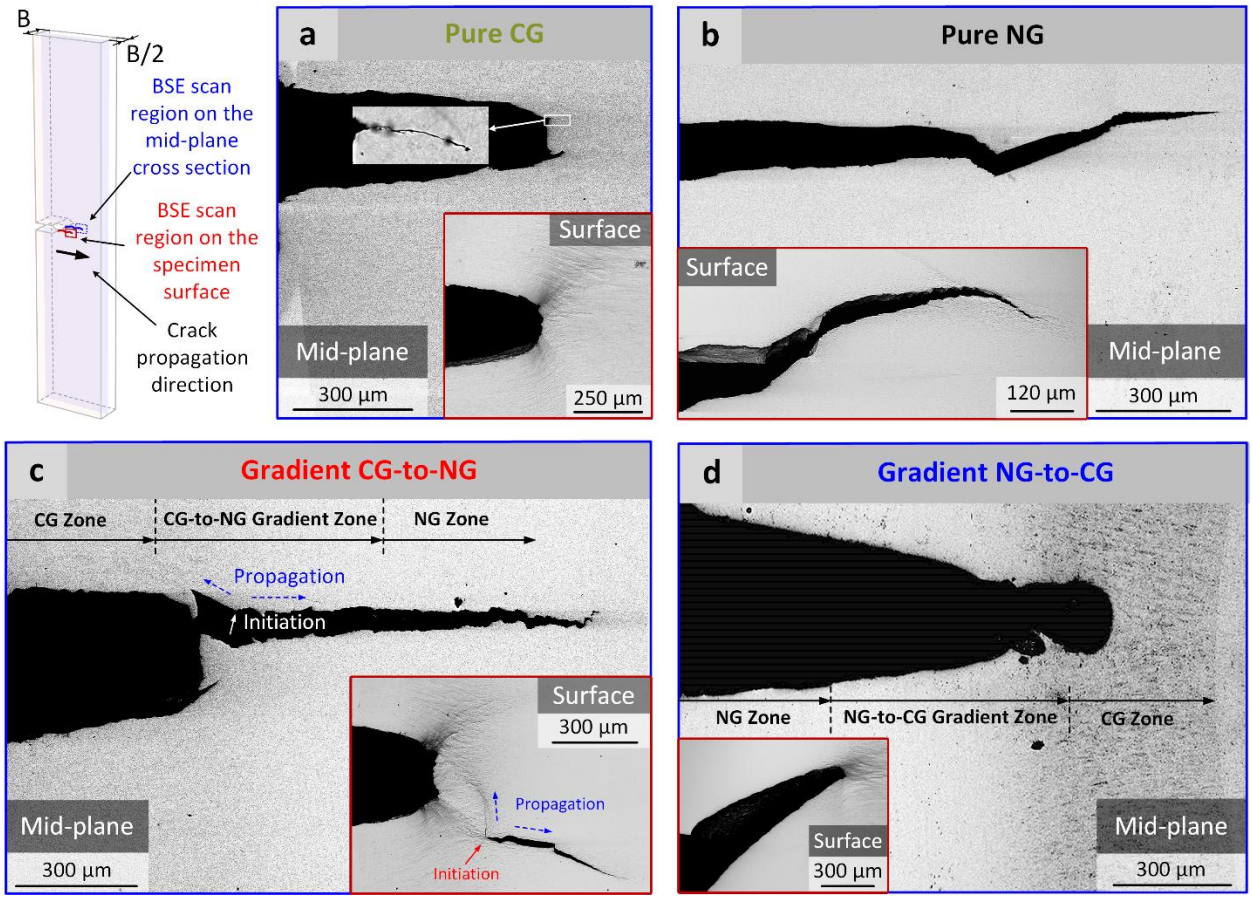


**FIGURE 7** Crack profiles characterized on the mid-thickness cross-section under plane-strain conditions. (a) CG specimen unloaded from a peak load of 367 N showing significant blunting at the crack tip. (b) Mode-I brittle crack profile in the NG specimen. (c) Blunted ductile crack ended in the initial part of the CG→NG zone, followed by a brittle crack initiated away from the blunted crack front. (d) Brittle crack initiated from the NG zone which arrested in the gradient NG→CG zone and the CG zone due to substantial crack-tip blunting in the CG region.

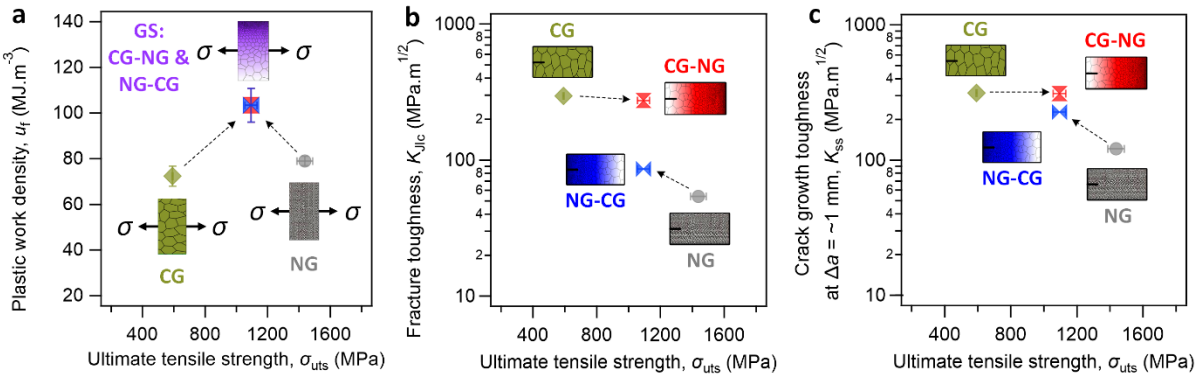


**FIGURE 8** Strength *vs.* toughness. (a) Plot showing the plastic work density during uniaxial tensile fracture as a function of the ultimate strength, (b) Ashby map showing the fracture toughness $K_{JIc}$ at crack initiation as a function of the ultimate tensile strength for the CG, NG, CG→NG, and NG→CG Ni structures, and (c) Ashby map showing the crack growth fracture toughness $K_{ss}$ at $\Delta a$ ~ 1 mm as a function of the ultimate tensile strength for the CG, NG, CG→NG, and NG→CG Ni structures.

**TABLE 1** Mechanical properties of the uniform grain-sized pure NG and pure CG structures, and gradient structured (CG→NG and NG→CG) Ni at room temperature.

| | **NG** | **NG→CG** | **CG** | **CG→NG** |
|---|---|---|---|---|
| Yield strength, $\sigma_y$ (MPa) | 1095 ± 66 | 687 ± 59 | 383 ± 3 | 687 ± 59 |
| Ultimate tensile strength, $\sigma_{uts}$ (MPa) | 1437 ± 50 | 1094 ± 38 | 592 ± 4 | 1094 ± 38 |
| Elongation to failure, $\varepsilon_f$ | 6.6 ± 0.1% | 11.0± 0.4% | 14.2 ± 0.6% | 11.0 ± 0.4% |
| Plastic work density (or work of fracture), $u_f$ (MJ.m$^{-3}$), area under the true stress-plastic strain curve | 79.0 ± 2.1 | 103.4 ± 7.4 | 72.4 ± 4.4 | 103.4 ± 7.4 |
| Scaling constant $C_1$ in the power law relationship of the *J*-R($\Delta a$) curve | 64.2 | 223 | 498 | 469.8 |
| Hardening exponent $C_2$ in the power law relationship of the *J*-R($\Delta a$) curve | 1 | 1.25 | 0.46 | 0.35 |
| Provisional *J*-integral at crack initiation, $J_Q$ (kJ.m$^{-2}$) | 13.2 | 33.4 | 396 | 338.6 |
| Provisional fracture toughness at crack initiation, $K_Q$ (MPa.m$^{½}$) | 54.1 | 86.0 | 296.2 | 273.9 |
| Crack growth *J*-integral at $\Delta a$ = ~1 mm, $J_{ss}$ (kJ.m$^{-2}$) | 66.3 | 231.9 | 442.5 | 436.0 |
| Crack growth toughness at $\Delta a$ = ~1 mm, $K_{ss}$ (MPa.m$^{½}$) | 121.2 | 226.7 | 313.1 | 310.8 |
| | ASTM "valid" * | | ASTM "invalid" * | |

*According to ASTM Standard 1820, for the provisional toughness $J_Q$ to be considered as a size-indepdent fracture toughness ($J_{Ic}$), the validity requirements for the *J*-field dominance and plane-strain conditions shall be respectively met, *i.e.* ,that $b_0, B > 10J_Q/\sigma_0$, where the $b_0$ and $B$ are the initial ligament length and the specimen thickness, respectively. The flow, or effective yield, stress, $\sigma_0 = ½ (\sigma_y + \sigma_{uts})$, is 1266 MPa, 488 MPa, and 891 MPa for the NG, CG, and GS samples, respectively. The calculated $10J_Q/\sigma_0$ values for NG, NG→CG, CG, and CG→NG samples are 0.1 mm, 0.37 mm, 8.11 mm, and 3.8 mm. The $J_Q$ and $K_Q$ of NG and NG→CG samples satisfy the specimen size requirements, $b_0, B > 10J_Q/\sigma_0$, and thus they are regarded as ASTM valid $J_{Ic}$ and $K_{JIc}$. Both CG and CG→NG samples do not meet the validity requirements.

## Appendix A. Supplementary Data

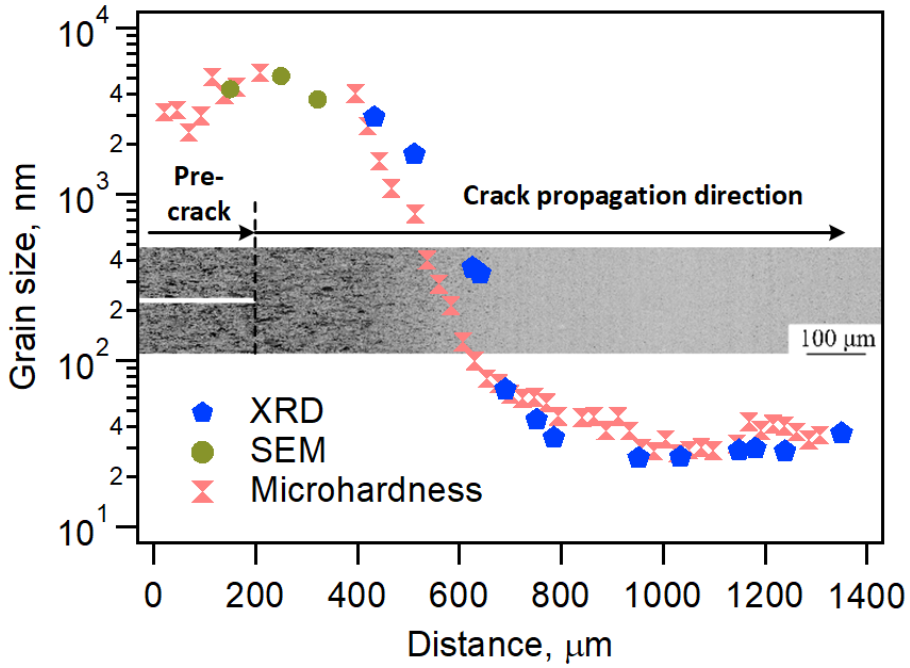


**FIGURE A.1** Comparison of grain size measurements by x-ray diffraction (XRD), scanning electron microscopy (SEM), and microhardness profiling methods. The validation of determining the grain size distribution from the microhardness profile by the Hall-Petch relationship was checked by direct measurement of the grain size using XRD with Cu-Ka radiation. Gradient Ni plate was mechanically polished layer by layer along the deposition direction. The XRD pattern scanned on the polished sample surface was analyzed to derive the grain size based on the full width at half maximum (FWHM) using Scherrer formula after correcting the instrumental line broadening. For the columnar coarse grains, whose sizes are larger than ~2 μm in the traverse direction, the grain sizes were checked by SEM imaging using the linear intercept method.

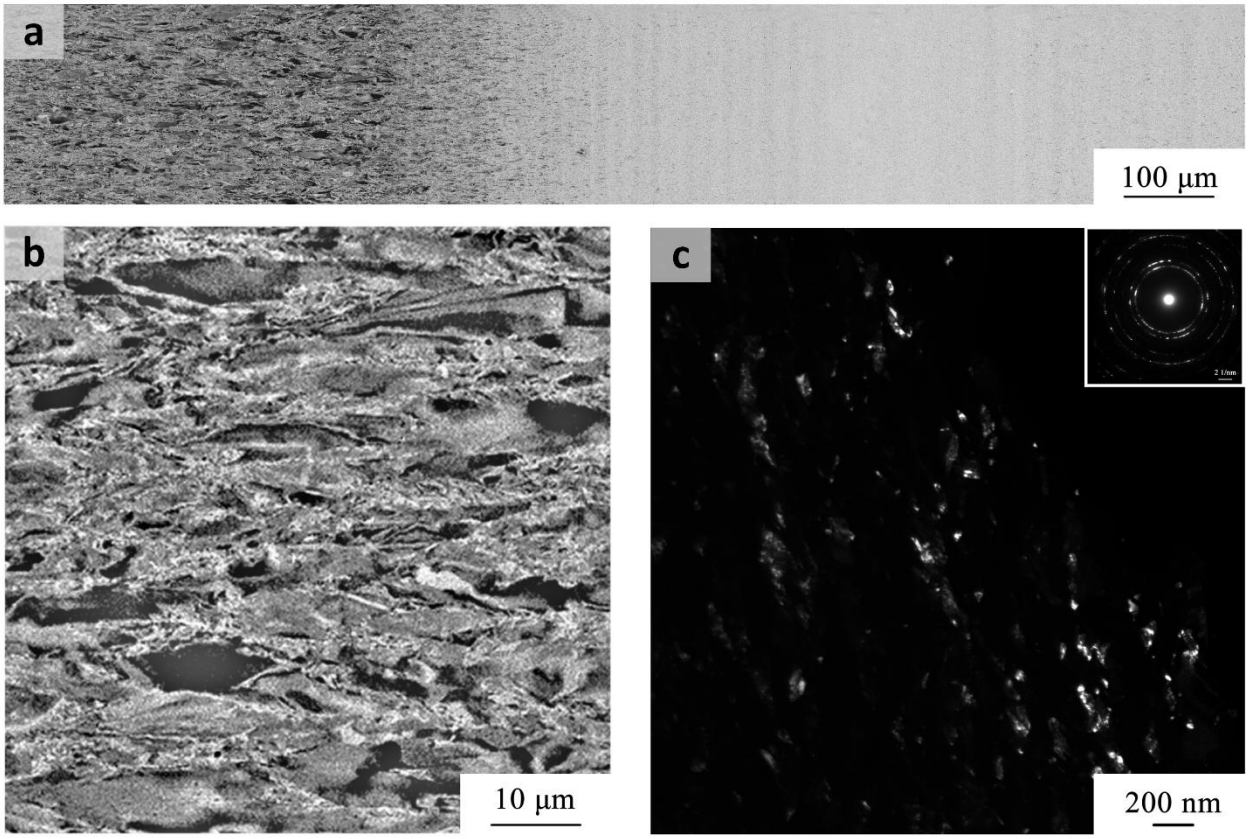


**FIGURE A.2** (a) Cross-sectional SEM images of the gradient structure. (b) Representative SEM image of the coarse grains on the CG side. (c) Dark-field TEM image of the nano-grains on the NG side. The inset shows the corresponding selected area electron diffraction (SAED) pattern.

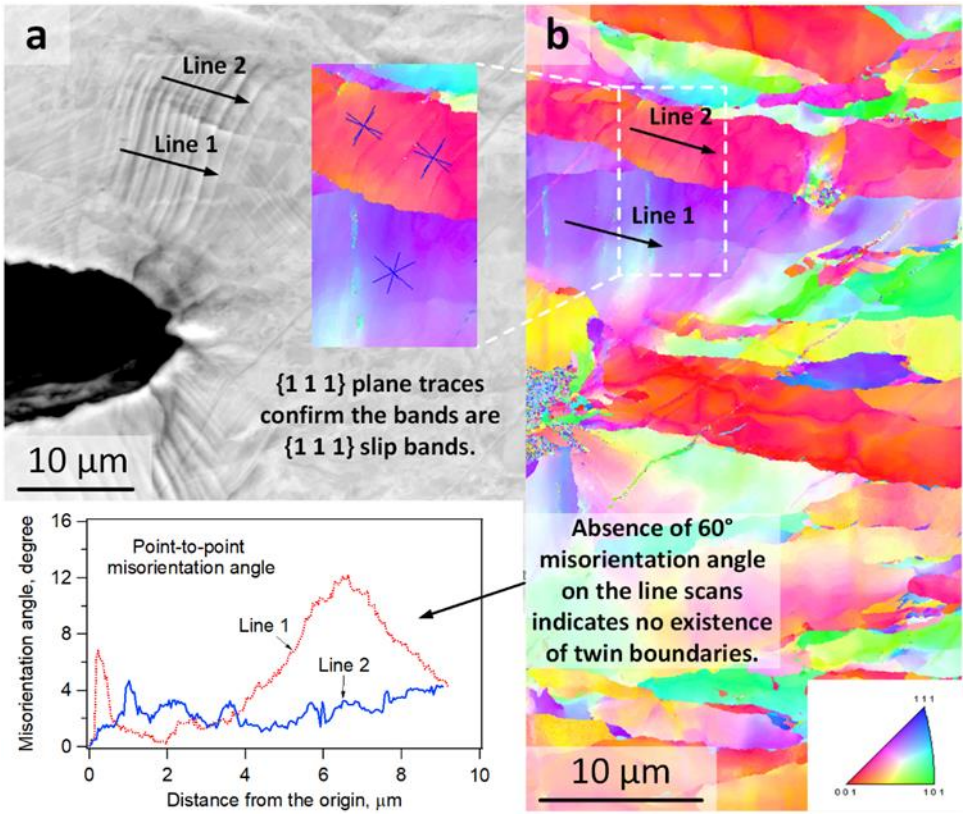


**FIGURE A.3** Confirmation of deformation modes as dislocation slip, rather than deformation twinning, in the vicinity of the blunted crack tip in the coarse-grained zone. Backscattered electron (BSE) and electron backscattered diffraction (EBSD) imaging on the region ahead of the blunted crack tip in the CG specimen show that multiple shear bands are formed in favorably-orientated coarse grains. The misorientation angle distributions along the two lines drawn across the shear bands display an absence of 60° misorientation angle, which indicates the non-existence of twin boundaries. Plane trace analysis further reveals these shear bands align with {1 1 1} plane traces projected on the specimen surface, confirming these shear bands are {1 1 1} slip bands.